Article

Not peer-reviewed version

The Effect of Applied Hydrostatic Pressures in Ferromagnetic Ordered HoM2 [M = (Al, Ni)] Laves Phases: A DFT Study

Tomás López-Solenzal , David Ríos-Jara , Manuel Ramos , César Fidel Sánchez-Valdés *

Posted Date: 3 September 2025

doi: 10.20944/preprints202509.0255.v1

Keywords: $HoNi_2$ and $HoAl_2$ Laves phases; Density Functional Theory (DFT); Hubbard U correction calculations (DFT+U); hydrostatic pressure effect on magnetic properties

Article

The Effect of Applied Hydrostatic Pressures in Ferromagnetic Ordered HoM_2 [M = (Al, Ni)] Laves Phases: A DFT Study

T. López-Solenzal [1], D. Ríos-Jara [2], M. Ramos [1] and C.F. Sánchez-Valdés [1,*]

[1] Departamento de Física y Matemáticas, Instituto de Ingeniería y Tecnología, Universidad Autónoma de Ciudad Juárez, 450N Avenida del Charro, Ciudad Juárez, Chihuahua, México, 32310

[2] Instituto Potosino de Investigación Científica y Tecnológica A.C., Camino a la Presa San José 2055, Col. Lomas 4ª sección, San Luis Potosí, S.L.P. 78216, México

* Correspondence: cesar.sanchez@uacj.mx; Tel.: +52-656-688-4887

Abstract

In this study, Density Functional Theory (DFT) with Hubbard U correction calculations (DFT+U) were used to examine the ferromagnetic properties of HoM_2 Laves phases (M = {Al, Ni}) under external hydrostatic pressure from 0 GPa to 1.0 GPa. The resulting net magnetic moments of 8.61 μ_B ($HoAl_2$) and 8.12 μ_B ($HoNi_2$) align with values reported in experiments. Additionally, for both alloys, the ferromagnetic behavior remains unchanged under applied pressures from 0 GPa to 1.0 GPa. The study also confirms that the magnetic properties of the alloys are mainly influenced by the 4f electrons; 3d electrons have a slightly more significant role in $HoNi_2$ Laves phases compared to $HoAl_2$. The contribution of electrons in *d* and *f* orbitals to the net magnetic moment of each Laves phase alloy within the specified pressure range was examined. Furthermore, the crystal geometry optimization and electronic specific heat coefficient were calculated as functions of applied pressures up to 1.0 GPa for both ferromagnetically ordered Laves phases.

Keywords: $HoNi_2$ and $HoAl_2$ Laves phases; Density Functional Theory (DFT); Hubbard U correction calculations (DFT+U); hydrostatic pressure effect on magnetic properties

1. Introduction

Experimental and theoretical research in the field of magnetocaloric-based cooling has grown over the past 25 years due to the higher energy efficiency and environmentally friendly nature of this cooling technology compared to the conventional one based on the expansion and compression of gases [1–6]. In the last few years, the interest in developing magnetic refrigerators for hydrogen liquefaction has encouraged important efforts to find, synthesize, and assess the magnetocaloric response of many families of rare earth (R) based alloys due to the significant magnetocaloric response of many compounds below the precooled reference temperature of 77 K [7–9]. Among all the alloy systems investigated, the cubic Laves phases in the RM_2 systems with M = {Al, Ni} stand out due to the remarkable magnetocaloric properties, especially for the heavy R elements as Ho, and Er [6–10].

Density functional theory (DFT) is a fundamental computational method in materials science, providing atomistic insights into crystals and molecules. By resolving a material's electronic structure, it enables the investigation and prediction of structure–property relationships and the underlying physicochemical phenomena in solids [11–15]. These compounds crystallize into the $MgCu_2$-type structure (C15, space group: Fd–3m) [10], with a lattice parameter of 7.810 Å for $HoAl_2$ and 7.130 Å for $HoNi_2$ [16,17], and show Weiss-Curie temperatures T_C of 29 K and 13.4 K, respectively [18,19]. Two lattice-related characteristics of Laves phases (AB_2) are that the relationship between the atomic radii of A and B atoms is between 1.05 and 1.68, and that for an atomic radius ratio (r_A/r_B) of

 doi:10.20944/preprints202509.0255.v1

1.225, the crystal structures have a higher packing density (around 71%) [10,20–24]. Green hydrogen economy needs the hydrogen storage due to hydriding properties in cell unit of Laves C15 phases. Laves intermetallics can be used to store interstitially the hydrogen by offering different positions (i.e., 3 tetrahedral interstices) [20].

Furthermore, $HoAl_2$ exhibits magnetic anisotropy characterized by the easy magnetization axis being <110> for temperatures below 20 K; above this temperature, the easy axis shifts to the <100> intermediate direction [18,25]. Additionally, a spin reorientation occurs at T = 20 K. The hard magnetizations axis in $HoAl_2$ is <111> crystal direction [19,25]. The directions of the easy, intermediate, and hard magnetization axes of $HoNi_2$ are <100>, <110>, and <111>, respectively [17,25–28].

The present work investigates, through Density functional theory with Hubbard U correction calculations (DFT+U), the effect of hydrostatic pressure on the electronic and magnetic properties of the ferromagnetically ordered $HoAl_2$ and $HoNi_2$ Laves phases. The spin polarization calculations are performed along <001> crystal direction. We systematically explore how electronic density of states are affected the in the $HoAl_2$ and $HoNi_2$ alloys. The theoretical calculations indicate significant changes in the electronic structure under a small hydrostatic pressure of 0.1 GPa in $HoNi_2$. A multicaloric approach in the solid-state cooling technology based on the magneto-caloric and baro-caloric effects has been used [2,3]. The combination of different external fields (e.g., magnetic field and hydrostatic pressure) allows an enhancement of caloric response by tailoring the magnetic moment (related to electronic density of states) with the pressure during the magnetic phase transition. Our finding is that the net magnetic moment can be modified (drops a 22.5 %) after a 0.1 GPa hydrostatic pressure is applied. To our knowledge, the electronic and magnetic properties from ab-initio calculations under hydrostatic pressure in $HoAl_2$ and $HoNi_2$ have not yet been reported to date.

2. Materials and Methods

The present study was performed using Cambridge Serial Total Energy Package (CASTEP) within density functional theory framework, using BIOVIA-Materials Studio®. For the exchange-correlation, the revised Perdew-Burke-Ernzerhof (RPBE) functional was applied as part of the generalized gradient approximation (GGA). It's known that the GGA method fails to correctly describe the localized 4*f* and 3*d* electrons; therefore, the DFT+U (U-Hubbard) correction was introduced into calculations [29–31]. It is important to note that U corrections within the GGA approximation show better accuracy to investigating the magnetic and electronic structures of 4*f* and 3*d* compounds compared to the local density approximation (LDA) or hybrid functionals [32,33]. The U values of localized electrons were 2.50 eV and 6.0 eV for Ni and Ho atoms, respectively. The U value was set to 0 eV for Al atoms because the lack of localized electrons. To calculate the electronic density of states (DOS), a 13 × 13 × 13 k-mesh generated by the Monkhorst-Pack scheme was used to integrate the Brillouin zone. For the plane-wave propagation along the crystal, a cut-off energy of 500 eV was applied [34–37]. The charge convergence criteria was set at 1×10^{-6} eV for self-consistent field cycles. During the geometric optimization process, the compressive external stress was applied along the a, b, and c axes to consider the effect of external hydrostatic pressure using Broyden–Fletcher–Goldfarb–Shanno (BFGS) algorithm.

The stoichiometric HoM_2 with M = {Al, Ni} Laves phases crystallize in a cubic $MgCu_2$-type structure with a space group Fd–3m. **Figure 1** schematically shows the crystalline and magnetic structure and primitive cell of HoM_2 (M = {Al, Ni}) Laves phases. In the AB_2 structure, the A atom (i.e., Ho) occupies the 8a Wyckoff site at (0 0 0), while the B atoms (i.e., Al and Ni) occupy the 16a Wyckoff site at (5/8 5/8 5/8) positions. For Al, Ni, and Ho, the electronic configuration is described as [Ne] $3s^2\ 3p^1$, [Ne] $3s^2\ 3p^6\ 3d^8\ 4s^2$, and [Ne] $3s^2\ 3p^6\ 3d^{10}\ 4s^2\ 4p^6\ 4d^{10}\ 5s^2\ 5p^6\ 4f^{11}\ 6s^2$, respectively. It is important to note that for simulating $HoAl_2$ and $HoNi_2$ Laves phases, we used experimental lattice parameters instead of those obtained from minimizing the total energy as a function of volume for the crystalline structures. The used lattice parameters $a = b = c$ were 7.810 Å for $HoAl_2$ and 7.130 Å for

 doi:10.20944/preprints202509.0255.v1

$HoNi_2$ [16,17]. The ferromagnetic ordering of each compound was modeled assuming that only the rare earth atoms, specifically Ho at 8a positions, possess a magnetic moment aligned along the <001> direction. Zero magnetic moment was assumed for Al and Ni atoms, which are located at 16a positions.

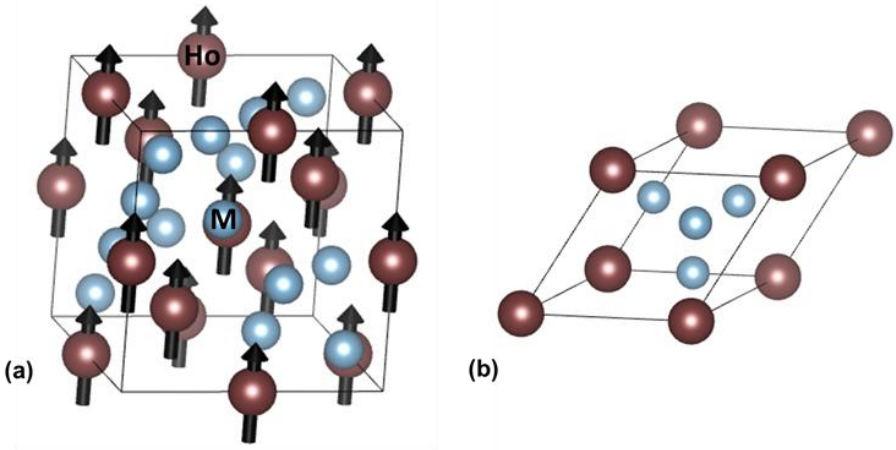

Figure 1. Schematic representation of the $MgCu_2$ cubic crystal structure **(a)** and primitive cell (rhombohedral trigonal) **(b)** of the ferromagnetically ordered $HoAl_2$ and $HoNi_2$ Laves phases. The silver and brown spheres represent the elements Al or Ni, and the rare earth element Ho, respectively. The black arrows show that the Ho magnetic moment points along the c-axis.

3. Results and Discussion

3.1. Electronic Properties

Table 1 displays the lattice parameter and interatomic distances between Al-Al, Ho-Al, and Ho-Ni in the Laves phases HoM_2 with M = {Al, Ni}, under applied hydrostatic pressures from 0 GPa to 1.0 GPa. It is worth noting that $HoAl_2$ is more sensitive to external pressure than the $HoNi_2$ alloys. The structural stability of both $HoAl_2$ and $HoNi_2$ remains unchanged across the entire range of applied pressures. Their corresponding formation energy E_f values at P = 0 GPa are -9.485×10^3 eV ($HoAl_2$) and -13.47×10^3 eV ($HoNi_2$). For non-zero pressures, the overall magnetic behaviors do not exhibit significant variation due to the minimal compaction in their crystal structures. All formation energy values remained nearly constant with a virtually negligible increase (less than 1%) under external pressures up to 1.0 GPa; details are shown in **Figure A1** in the Appendix section. Additionally, substituting Al atoms with Ni atoms leads to a reduction in lattice parameters, resulting in an increase in bulk modulus at applied pressures around 1.0 GPa, as detailed in **Table 1**.

Table 1. Diagonal component σ_{ij} of stress tensor, bulk modulus B, primitive unit cell volume V_P (i.e., rhombohedral trigonal), the compressive stress Δ, and interatomic Al-Al, Ho-Al, and Ho-Ni distances obtained for the $HoAl_2$ and $HoNi_2$ Laves phases under applied hydrostatic pressures of 0 GPa ≤ *P* ≤ 1.0 GPa.

Alloy	$HoAl_2$							$HoNi_2$					
P (GPa)	B (GPa)	σ_{ij} (GPa)	a (Å)	$d_{Al\text{-}Al}$ (Å)	$d_{Ho\text{-}Al}$ (Å)	V_P (Å^3)	Δ (%)	B (GPa)	σ_{ij} (GPa)	a (Å)	$d_{Ni\text{-}Ni}$ (Å)	$d_{Ho\text{-}Ni}$ (Å)	V_P (Å^3)	Δ (%)
0.0	40.66	−0.00005	5.652	2.826	3.314	127.675	0.000	49.79	−0.00115	5.262	2.631	3.086	103.066	0.000
0.1	45.68	−0.10067	5.646	2.823	3.311	127.299	−0.294	56.58	−0.10030	5.258	2.629	3.083	102.840	−0.219
0.2	52.56	−0.19968	5.640	2.820	3.307	126.908	−0.600	58.98	−0.19724	5.255	2.628	3.081	102.655	−0.399
0.3	56.69	−0.29771	5.635	2.818	3.304	126.533	−0.894	60.33	−0.30162	5.252	2.626	3.080	102.480	−0.569

 doi:10.20944/preprints202509.0255.v1

0.4	58.00	−0.39932	5.629	2.815	3.301	126.165	−1.182	68.79	−0.40011	5.248	2.624	3.077	102.241	−0.801
0.5	60.58	−0.49793	5.623	2.812	3.297	125.780	−1.484	71.50	−0.50638	5.245	2.623	3.076	102.072	−0.964
0.6	64.07	−0.60178	5.618	2.809	3.294	125.380	−1.797	76.23	−0.60287	5.242	2.621	3.074	101.868	−1.162
0.7	65.22	−0.70149	5.613	2.807	3.291	125.055	−2.052	82.56	−0.69933	5.239	2.620	3.072	101.703	−1.322
0.8	66.65	−0.80276	5.607	2.804	3.288	124.681	−2.345	84.36	−0.80034	5.235	2.618	3.070	101.479	−1.540
0.9	68.37	−0.89994	5.602	2.801	3.285	124.328	−2.621	91.47	−0.89917	5.232	2.616	3.068	101.321	−1.693
1.0	70.89	−0.99911	5.597	2.799	3.282	123.992	−2.884	98.45	−0.99998	5.229	2.615	3.066	101.132	−1.876

3.2. Determination of Electronic Coefficient in Specific Heat Capacity

Considering that each atom donates one electron to the Fermi gas in the solid, the free-electron number densities (N/V) for $HoAl_2$ and $HoNi_2$ are 1.678×10^{28} m^{-3} and 2.203×10^{28} m^{-3}, respectively. On the other hand, M($HoAl_2$) = 218.894 g/mol, ρ($HoAl_2$) = 6.08 g/cm^3 [16], M($HoNi_2$) = 282.316 g/mol, and ρ($HoNi_2$) = 10.33 g/cm^3 [38] were used.

Bearing in mind that in metals theory at P = 0 GPa and T = 0 K, the Fermi energy E_F can be calculated as follows:

$$E_F = \frac{h^2 {k_B}^2}{2 m_e} \left(\frac{3 N}{8 \pi V}\right)^{2/3} \quad (1)$$

where h and k_B are the Planck and Boltzmann constants, respectively, and m_e is the electron mass. Using equation (1) and previous values, the Fermi temperature T_F can be calculated through the formulae:

$$T_F = \frac{E_F}{k_B} \quad (2)$$

The electronic coefficient γ_e of specific heat capacity can be calculated using the following equation:

$$\gamma_e = \frac{\pi^2 k_B N_A}{3 T_F} \quad (3)$$

The calculated values of Fermi energy and its temperature, and the electronic coefficient γ_e using the equations (1), (2), and (3) are listed in **Table 2**. The N/V, E_F and T_F values agree with those obtained for other elements such as K (i.e., 1.40×10^{28} m^{-3}; 2.13 eV; 2.47×10^4 K), Ag (i.e., 5.86×10^{28} m^{-3}; 5.53 eV; 6.41×10^4 K), and Cu (i.e., 8.47×10^{28} m^{-3}; 7.06 eV; 8.19×10^4 K) [39].

Table 2. The calculated values of Fermi energy (E_F), Fermi temperature (T_F) and the electronic specific heat capacity coefficient (γ_e) obtained by the equations (1), (2), and (3) for both Laves phases ($HoAl_2$ and $HoNi_2$).

Laves phases	E_F (eV)	T_F (10^{-4} K)	γ_e (10^{-3} J mol^{-1} K^{-2})
$HoAl_2$	2.392	2.777	1.476
$HoNi_2$	2.869	3.331	1.231

Another way to determine the electronic heat capacity coefficient γ_e for alloys is through DFT quantum calculations. The Einstein-Debye model states that $c_p(T) = \gamma_e T + \beta_{ph} T^3$ at temperatures $T \ll T_D$, where T_D is the Debye temperature, and the terms $\gamma_e T$ and $\beta_{ph} T^3$ represent the electronic and phonon contributions to the specific heat capacity, respectively. From the Sommerfeld approximation [40], the coefficient γ_e can be calculated as follows:

$$\gamma_e = \frac{\pi^2 {k_B}^2}{3} \Delta n(E_F) \quad (4)$$

where $\Delta n(E_F)$ is the density of electrons per eV at the Fermi level. This expression applies when external hydrostatic pressure is considered.

Figure 2 shows how the electronic specific heat capacity coefficients, calculated by eq. (4), change with increasing external hydrostatic pressures up to 1.0 GPa for the studied Laves phases. For $HoAl_2$, the obtained γ_e value at P = 0 GPa is 9.43×10^{-3} J mol^{-1} K^{-2}. This result differs from that obtained

 doi:10.20944/preprints202509.0255.v1

through the electron gas model in metals (**Table 2**); the values tend to slightly increase, reaching an average of 10.02 × 10^{-3} J mol^{-1} K^{-2} as the applied pressure increases. Conversely, the initial value for the $HoNi_2$ alloys at 0 GPa (i.e., 3.87 × 10^{-3} J mol^{-1} K^{-2}) is like the value calculated using the gas model in metals; see **Table 2** for details (1.231 × 10^{-3} J mol^{-1} K^{-2}). Later, it increases noticeably to 8.02 × 10^{-3} J mol^{-1} K^{-2} with an applied pressure of 0.1 GPa and then remains nearly constant at an average value of 8.05 × 10^{-3} J mol^{-1} K^{-2}. At non-zero pressures, the obtained values for $HoAl_2$ and $HoNi_2$ are closer to each other, as calculated by DFT+U modelling.

Von Ranke *et al*. reported electronic specific heat capacity coefficients of 10.6 × 10^{-3}, 5.5 × 10^{-3}, 4.8 × 10^{-3} and 4.6 × 10^{-3} J mol^{-1} K^{-2} for $LaAl_2$, $LuAl_2$, $LaNi_{2.2}$, and $LuNi_2$, respectively [41]. De Oliveira and colleagues reported a γ_e experimental value of 5.4 × 10^{-3} J mol^{-1} K^{-2} from the $c_p(T)$ curve for non-ferromagnetic $LuAl_2$ stating that this alloy shows the same structure as $HoAl_2$, and a similar γ_e value [42]. Campoy et al. experimentally determined a value of γ_e = 7.0 × 10^{-3} J mol^{-1} K^{-2} for a bulk polycrystalline $HoAl_2$ alloy from $c_p(T)$ data [43]. The DFT and Fermi gas approach of γ_e values at P = 0 GPa for the Laves phases alloys agree with experimental ones obtained by cp(T) data.

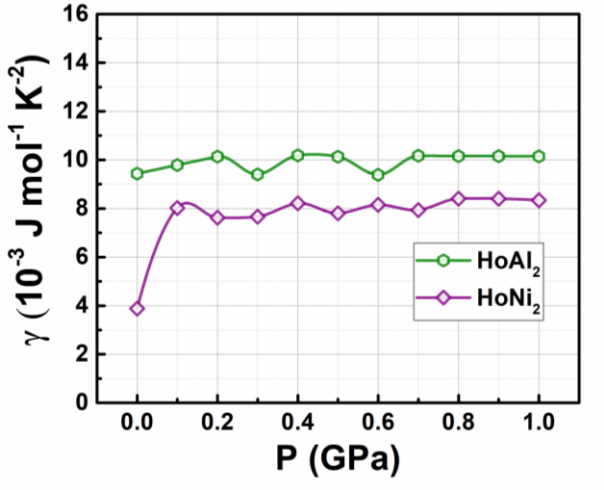

Figure 2. Electronic specific heat capacity coefficient as a function of the applied hydrostatic pressure for $HoAl_2$ and $HoNi_2$ alloys.

3.3. Electronic Density of States

3.3.1. Total Density of Electronic States at P = 0 GPa

Figure 3 shows the total density of electronic states (DOS) obtained in ferromagnetically ordered crystal structures HoM_2 with M = {Al, Ni} Laves phases. The electronic structure for both compounds, *s* and *p* orbitals, is nearly symmetric and localized at deeper energies compared to *d* and *f* orbitals, which are at the Fermi level. The *s* orbitals are localized among –49.00 eV and –48.00 eV with a maximum of electronic density of 3.92 e^-/eV at –48.59 eV for $HoAl_2$. When the post-transition metal (Al) is replaced by a transition metal (Ni), the localization of *s* orbitals shifts toward higher energies (i.e., between –47.43 eV and –46.19 eV) with a similar electronic density of 3.87 e^-/eV. The *p* orbitals in $HoAl_2$ are localized in the energy range of –24.30 eV ≤ E – E_F ≤ –22.62 eV, while they are positioned between –23.00 eV and –21.32 eV for $HoNi_2$. Our calculations showed that the spin-up channel is shifted to lower energies compared to the spin-down channel while maintaining symmetry between them for both alloys. It is important to note that substituting Al with Ni reduces the maximum value in the DOS of p bands from 9.53 e^-/eV to 5.95 e^-/eV, and the DOS curve tends to flatten into a double peak, see the **Figures 3(a)-3(b)**.

The *d* and *f* orbitals are very close to the Fermi level. Specifically, *d* bands range from –5.2 eV to 10.0 eV, while *f* bands range from –5.3 eV to 3.0 eV. Both the DOS of *d* and *f* orbitals exhibit a notable asymmetry. Additionally, *f* bands are the most populated in both compounds. Therefore, the

 doi:10.20944/preprints202509.0255.v1

localized *f* electrons continue to be responsible for ferromagnetic order in HoM_2 (M = {Al, Ni}) Laves phases. Replacing the post-transition metal Al with Ni leads to symmetry collapse of d orbitals, causing hybridization among *d* and *f* bands. This suggests that the magnetic behavior of $HoAl_2$ arises from localized electrons in *f* orbitals, and both itinerant and localized electrons in *d* and *f* orbitals contribute to ferromagnetism in $HoNi_2$.

The total magnetic moments along the <001> c-axis obtained for ferromagnetically ordered $HoAl_2$ and $HoNi_2$ Laves phases are 8.61 μ_B/f.u. and 8.12 μ_B/f.u., respectively. These values, derived from DOS, match the single crystalline data previously reported in scientific literature: 9.15 μ_B/f.u. to 9.18 μ_B/f.u. for $HoAl_2$ [18,25] and 8.52 μ_B/f.u. for $HoNi_2$ [19]. As summarized in **Table 3**, the net magnetic moment determined for polycrystalline ribbons [16,17], and bulk/massive [44,45] samples is close to that obtained from DFT quantum calculations.

Table 3. Cell parameter *a*, calculated magnetic moment μ_T and magnetization of $HoAl_2$ and $HoNi_2$ compared with experimental data reported in the literature.

Laves phase	Alloy type	*a* (Å)	μ_T (μ_B/f.u.)	T_C (K)	M_S (Am^2kg^{-1})	magnetization axis	reference
$HoAl_2$	DFT+U framework	7.810	8.61 [a]	-	220 [a]	<001>; intermediate	this work
	single-crystal	7.816 [c]	9.18 [b]	31.5	235 [b]	<011>; easy	[18]
		7.838	9.15 [c]	29.0	234 [c]		[25]
	bulk polycrystalline	7.8024	7.86	27.0	201	close to <001>; intermediate	[44]
	polycrystalline ribbons	7.8109	7.08 [c,e]	24.0	181 [c,e]	close to <001>; intermediate	[16]
$HoNi_2$	DFT+U framework	7.130	8.12 [a]	-	161 [a]	<001>; easy	this work
	single-crystal	-	8.52 [d]	13.4	168 [d]	<001>; easy	[19]
	bulk polycrystalline	7.1318	8.40	22.0	167	very close to <001>; easy	[44,45]
	polycrystalline ribbons	7.1497	8.02 [c]	13.9	159 [c]	close to <001>; easy	[17]

Experimental data measured at temperature: [a] T = 0 K. [b] T = 4.2 K. [c] T = 2.0 K. [d] T = 1.4 K. [e] determined from **Figure A2**.
The crystal structure cell unit is reported to room temperature.

 doi:10.20944/preprints202509.0255.v1

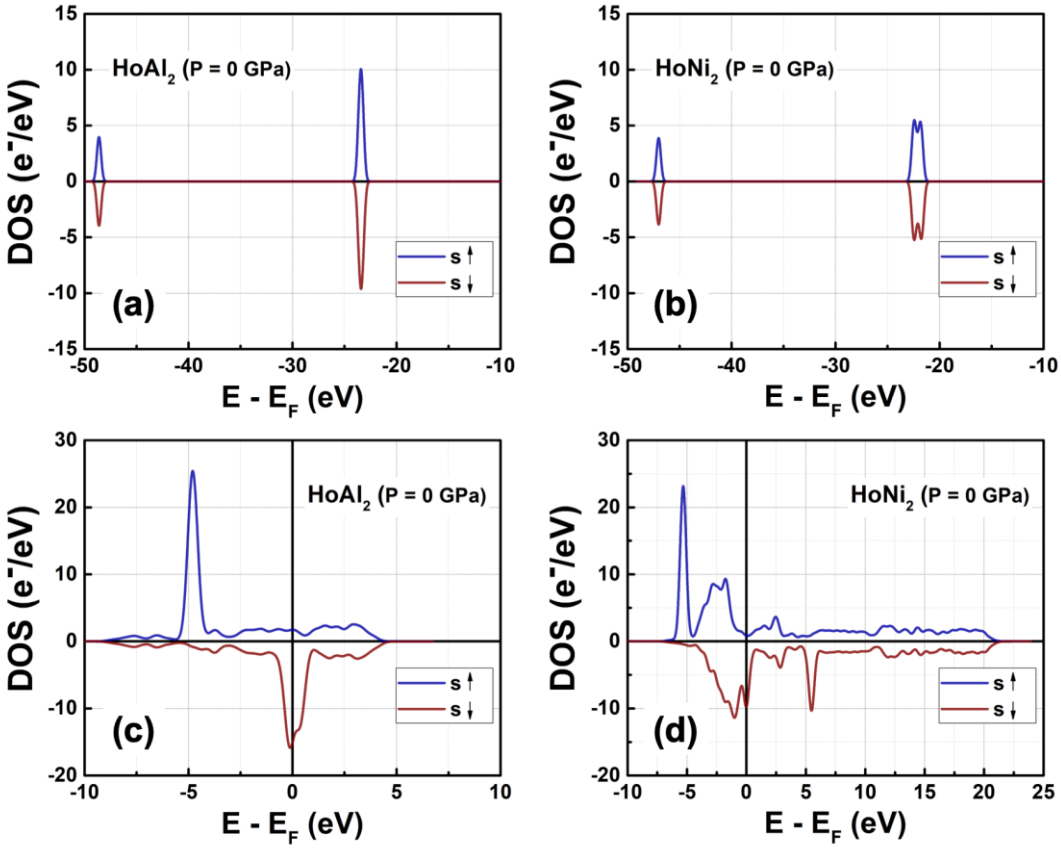

Figure 3. Total DOS at P = 0 GPa obtained for ferromagnetically ordered **(a)** $HoAl_2$ and **(b)** $HoNi_2$ compounds.

3.3.2. Total Electronic Density of States at 0 GPa < P ≤ 1.0 GPa

Figure 4 shows the calculated DOS for ferromagnetically ordered $HoAl_2$ and $HoNi_2$ Laves phases under external hydrostatic pressures from 0 GPa to 1.0 GPa. For both alloys, a small increase in the external pressure applied to the crystal structure causes a shift to higher energies of the *s* and *p* orbitals. The shift is more evident in $HoAl_2$ (**Figure 4(a)**) than in $HoNi_2$ (**Figure 4(b)**). Meanwhile, *d* and *f* orbitals move closer to the Fermi energy level. For $HoNi_2$, a significant redistribution occurs in the electronic population of *f*-orbitals at non-zero pressure; the maximum of the spin-up channel increases from 14.26 e^-/eV to 23.48 e^-/eV, while the initial splitting of the spin-down channel disappears, and a maximum electronic density of –14.35 e^-/eV is observed.

 doi:10.20944/preprints202509.0255.v1

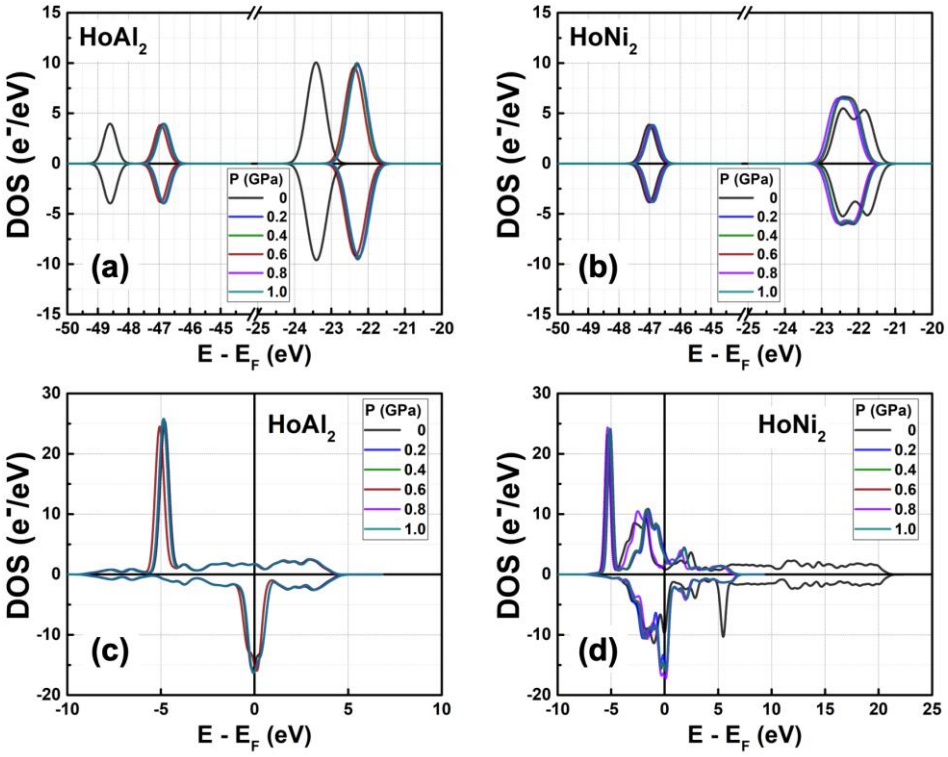

Figure 4. Total DOS obtained for ferromagnetically ordered **(a)** $HoAl_2$ and **(b)** $HoNi_2$ crystal structures under externals hydrostatic pressures between 0 GPa and 1.0 GPa. Selected curves are shown to provide visual insight.

Figure 5(a) shows the calculated total magnetic moment versus hydrostatic pressures in the range of 0 GPa ≤ P ≤ 1.0 GPa for ferromagnetically ordered HoM_2 (M = {Al, Ni}) crystal structures. For $HoAl_2$, the total magnetic moment remains nearly constant (around a mean value of 8.49 μ_B/f.u.) as applied pressure increases up to 1 GPa. On the contrary, for $HoNi_2$, the total magnetic moment at P = 0 GPa (8.12 μ_B/f.u.) decreases to 6.29 μ_B/f.u. at 0.1 GPa and then remains nearly constant for a non-zero applied pressure. This is a 22.5 % that DOS was modified after a 0.1 GPa, that can be useful in multicaloric approach during the magnetic phase transition [2,3]. Additionally, **Figure 5(b)** displays the calculated magnetic moment associated with *d* and *f* orbitals for both alloys. It is important to note that the magnetic order mainly results from localized *f* electrons. The itinerant electrons contribute only minimally to the magnetic moment. Moreover, for $HoNi_2$, the magnetic contribution of 4*f* electrons decreases from 7.45 μ_B/f.u. to 6.31 μ_B/f.u. under an applied pressure of 0.1 GPa and then remains nearly constant at a non-zero value pressures.

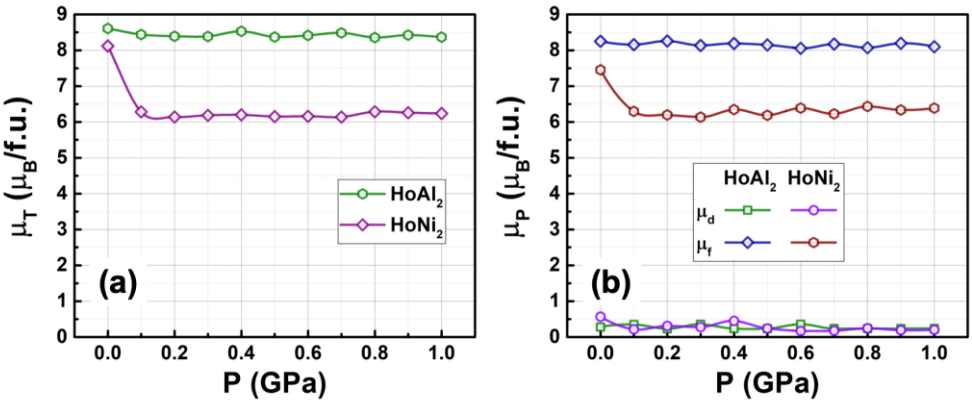

 doi:10.20944/preprints202509.0255.v1

Figure 5. (a) Total magnetic moment and **(b)** contributions from electrons in the *d* and *f* orbitals to the magnetic moment in ferromagnetically ordered $HoAl_2$ and $HoNi_2$ Laves phases, plotted as a function of external hydrostatic pressure (0 GPa ≤ P ≤ 1.0 GPa). The μ_T and μ_P values are obtained from the total and partial DOS, respectively.

3.3.3. Electronic Partial Density of States at P = 0 GPa

The obtained partial density of electronic states (PDOS) corresponding to *d* and *f* orbitals is shown in **Figure 6**. Once a transition metal like Ni replaces the post-transition metal Al in the crystalline structure, the electronic population of 3*d* electrons increases, while the density of electrons in 4f orbitals decreases, resulting in a broadened peak of the DOS curve. The contributions per orbital to the total magnetic moment are listed in **Table 4**. At P= 0 GPa, electrons localized at d orbitals contributed less to the net magnetic moment in the crystal structure $HoAl_2$ (i.e., 0.28 μ_B/f.u.) compared to $HoNi_2$ (i.e., 0.57 μ_B/f.u.). Therefore, the magnetic behavior of the ferromagnetically ordered $HoAl_2$ crystal structure is just due to unpaired electrons localized at *f* orbitals. When Al is fully replaced by Ni, the number of unpaired electrons in the *d* orbital increases; as a result, the magnetic moment of $HoNi_2$ arises from 3*d* and 4*f* electrons. Moreover, *s* and *p* orbitals shift to higher energies when Al is replaced by Ni, and *p* orbitals tend to decrease their maximum population, resulting in a broadened and flattened peak band. Partial DOS for *s* and *p* orbitals is shown in **Figure A3**. Finally, the contribution of electrons localized at *s* and *p* orbitals to the total magnetic moment is almost negligible for both alloys, $HoAl_2$ and $HoNi_2$.

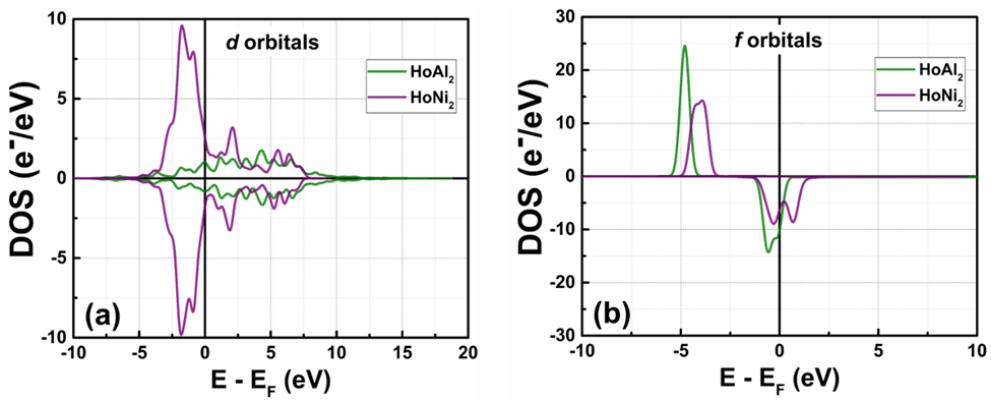

Figure 6. Partial DOS at P = 0 GPa obtained for **(a)** *d* and **(b)** *f* orbitals in the ferromagnetically ordered HoM_2 with M = {Al, Ni} Laves phases.

Table 4. Net magnetic moment values calculated using eq. (5) from the obtained DOS and compared with experimental data [18,19]. Electronic quantities with spin up and down, along with the difference in electronic states at the Fermi level, are shown for the ferromagnetically ordered $HoAl_2$ and $HoNi_2$ Laves phases along <001> direction.

Alloy	$n_{S\uparrow}(E_F)$ (e⁻/eV)	$n_{S\downarrow}(E_F)$ (e⁻/eV)	$\Delta n(E_F)$ (e⁻/eV)	$\mu_{S\uparrow}$ (μ_B/f.u.)	$\mu_{S\downarrow}$ (μ_B/f.u.)	μ_T^{DFT+U} (μ_B/f.u.)	μ_s (μ_B/f.u.)	μ_P (μ_B/f.u.)	μ_d (μ_B/f.u.)	μ_f (μ_B/f.u.)	μ_P (μ_B/f.u.)
$HoAl_2$	1.76	−15.10	−13.34	31.30	−22.69	8.61 †	−0.03	0.04	0.28	8.79	9.08
$HoNi_2$	14.59	−9.11	5.48	37.08	−28.96	8.12 ‡	0.11	−0.17	0.57	7.45	7.96

Experimental values of total magnetic moment μ_T^{exp}: † 9.18 μ_B/f.u. [18], and ‡ 8.52 μ_B/f.u. [19].

 doi:10.20944/preprints202509.0255.v1

On the one hand, **Figure 6(a)** shows that the 4*d* and 3*d* electrons of Ho in $HoAl_2$ are located very close to the Fermi level with a very low density of states. In contrast, the 4*f* electrons of Ho in the spin-up channel are situated at –4.77 eV, far from the Fermi level, while the 4*f* electrons in the spin-down channel are practically at the Fermi level (–0.7 eV); see **Figure 6(b)**. For $HoNi_2$, the 3*d* electrons in both spin-up and spin-down channels are near the Fermi level (at –1.75 eV). Conversely, the 4*f* electrons of Ho at the spin-up channel are localized at – 4.03 eV far away from the Fermi level; in the case of the spin-down channel, 4*f* electrons are very close to the Fermi level (from – 1.16 eV to 0 eV). Noticing that the amount of Ho 4*f* electrons in $HoAl_2$ has larger peaks in the density of states compared to the broad, lower peaks of Ho 4*f* electrons in $HoNi_2$. Finally, the Ni 3*d* electrons have a higher density of states compared to the Ho 4*d* and 3*d* electrons.

3.3.4. Electronic Partial Density of States at 0 GPa ≤ P ≤ 1.0 GPa

For ferromagnetically ordered HoM_2 (M = {Al, Ni}) Laves phases, the applied external hydrostatic pressure induces a shift in the energies of the *s*, *p*, *d*, and *f* bands. This shift is more noticeable for the *s* and *p* bands in $HoAl_2$ than in $HoNi_2$. The PDOS obtained for *s* and *p* orbitals are shown in **Figure A4** of the Appendix section.

Figure 7 displays the PDOS for the *d* and *f* orbitals under external hydrostatic pressures ranging from 0 GPa to 1.0 GPa. In the ferromagnetically ordered $HoAl_2$ Laves phase, the applied pressures (0 GPa to 1.0 GPa) cause a slight rearrangement of the 3*d* and 4*d* Ho spin-up and spin-down channel bands. See details in **Figure 7 (a)**. The 4*f* electrons of Ho in the spin-up channel, initially localized far from the Fermi level at –4.77 eV, move slightly closer to the Fermi level as pressure increases, reaching –4.34 eV at 1.0 GPa (**Figure 7 (b)**). Meanwhile, the 4*f* electrons in the spin-down channel, initially localized at –0.70 eV, nearly reach the Fermi level.

Figures 7(c) and **7(d)** illustrate that for $HoNi_2$, the 3*d* electrons of Ni in both spin-up and spin-down channels do not undergo significant changes as the external pressure increases from 0 GPa to 1.0 GPa. Furthermore, the 4*f* electrons of Ho, a rare earth element, in both spin-up and spin-down channels show an increase in their maximum electronic density under non-zero applied pressure. It is important to note that the initial splitting of the spin-down channel tends to disappear. External pressure causes a redistribution of the electronic population across the orbitals for both alloys, but the most affected orbitals are the 4*f* orbitals of $HoNi_2$. The maximum population of electrons with spin-up at *f* orbitals of $HoNi_2$ increases from 14.26 e^-/eV to 23.48 e^-/eV, and their electronic density of the spin-down channel rises to –14.35 e^-/eV near the E_F level, as shown in **Figure 7(d)**.

 doi:10.20944/preprints202509.0255.v1

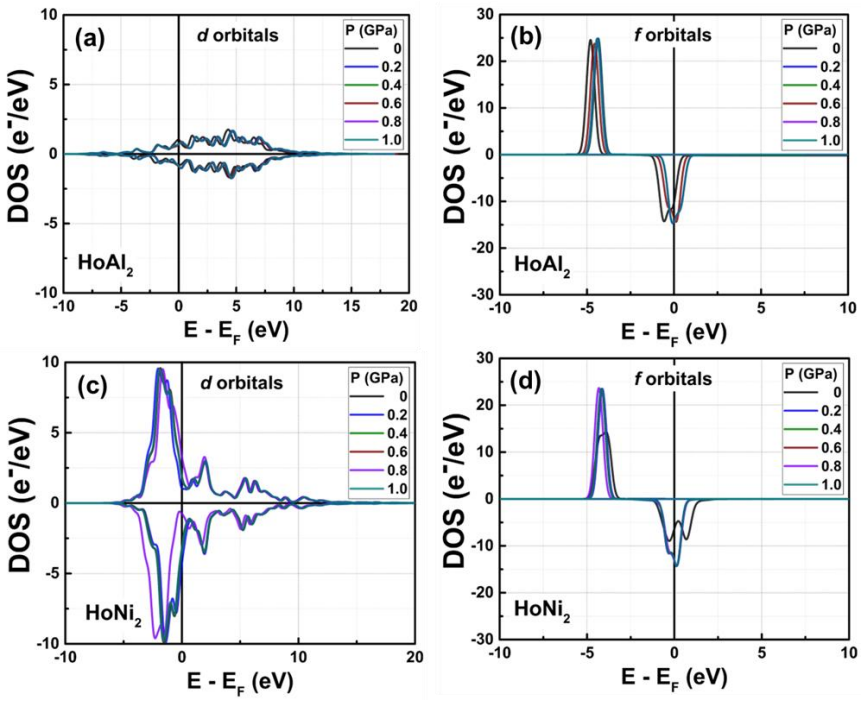

Figure 7. Partial DOS obtained for **(a)**, **(c)** d and **(b)**, **(d)** f orbitals of ferromagnetically ordered $HoAl_2$ and $HoNi_2$ crystal structures, respectively, under external hydrostatic pressures ranging from 0 GPa to 1.0 GPa (selected curves are shown for better visualization).

The net magnetic moment [40] was calculated using the following equation:

$$\mu_T = \int_{E_1}^{E_F} n_{S\uparrow}(E)\, dE \; - \int_{E_2}^{E_F} n_{S\downarrow}(E)\, dE \quad (5)$$

where E_1 and E_2 represent the starting energies of electronic states for spin-up and spin-down channels, respectively. **Table 4** presents the calculated net magnetic moment computed from the simulated DOS for ferromagnetically ordered $HoAl_2$ and $HoNi_2$ Laves phases, along with the contribution of electrons at *s*, *p*, *d*, and *f* orbitals to the total magnetic moment. When Al is fully replaced by Ni, the contribution of *d* electrons to the total magnetic moment slightly increases. Furthermore, the main contributor to magnetic behavior in ferromagnetically ordered HoM_2 with M = {Al, Ni} are the *f* electrons.

4. Conclusions

This study examined how hydrostatic pressures from 0 GPa to 1.0 GPa affect the crystal stability, electronic properties, and magnetic properties of ferromagnetically ordered $HoAl_2$ and $HoNi_2$ Laves phases through DFT+U calculations using the RPBE exchange-correlation functional within the GGA framework. All calculations were performed along the <001> direction, and the net magnetic moment obtained remains nearly constant for ferromagnetically ordered $HoAl_2$, with values of 8.61 μ_B per formula unit along the intermediate magnetization axis. The ferromagnetically ordered $HoNi_2$ Laves phases experience a reduction in their initial magnetic moment from 8.12 μ_B/f.u. to 6.29 μ_B/f.u. in the easy magnetization axis when subjected to non-zero applied pressure. The latter $HoNi_2$ Laves phase is useful for multicaloric approach in solid state cooling by using magneto-caloric and baro-caloric effects. The magnetic moment can be modified a 22.5 % under 0.1 GPa in the range of fully reversible loading and uploading regimes in the alloy when the hydrostatic pressure is applied and released, respectively. The most affected by the applied pressures was the $HoAl_2$ Laves phase, with a compressive stress of –2.88%, while the $HoNi_2$ exhibited a compressive stress of –1.87%. The interatomic distances change very little within the pressure range studied. The ferromagnetic order persists, displaying a reorganization of the electronic states, with the *f* orbitals of $HoNi_2$ Laves phases being the most affected. The stability of the ferromagnetically ordered $HoAl_2$ and $HoNi_2$ Laves

 doi:10.20944/preprints202509.0255.v1

phases' crystal structures remains unaffected across the entire range of applied pressures, and the formation energy stays constant up to 1.0 GPa.

Author Contributions: "Conceptualization, T. López-Solenzal and C.F. Sánchez-Valdés; methodology, T. López-Solenzal and C.F. Sánchez-Valdés; software, T. López-Solenzal, M. Ramos and C.F. Sánchez-Valdés; validation, T. López-Solenzal and C.F. Sánchez-Valdés.; formal analysis, T. López-Solenzal and C.F. Sánchez-Valdés; investigation, T. López-Solenzal, D. Ríos-Jara, Manuel Ramos and C.F. Sánchez-Valdés; resources, C.F. Sánchez-Valdés; data curation, T. López-Solenzal; writing—original draft preparation, T. López-Solenzal and C.F. Sánchez-Valdés; writing—review and editing, T. López-Solenzal, D. Ríos-Jara, M. Ramos, and C.F. Sánchez-Valdés; project administration, D. Ríos-Jara; funding acquisition, D. Ríos-Jara, M. Ramos, and C.F. Sánchez-Valdés. All authors have read and agreed to the published version of the manuscript."

Data Availability Statement: The data supporting this study's findings are available from the corresponding author upon reasonable request.

Acknowledgments: Authors also thank Instituto de Ingeniería y Tecnología of Universidad Autónoma de Ciudad Juárez for providing BIOVIA Materials Studio® licensing to perform all computational calculations. T. López-Solenzal thanks SECIHTI-México for doctoral scholarship 1072019. D. Ríos-Jara, C.F. Sánchez-Valdés and M. Ramos thank Sistema Nacional de Investigadores e Investigadoras fellowship of SECIHTI-México. APC was partially funded by 2025 Publich Program of Instituto de Innovación y Competividad del Gobierno del Estado de Chihuahua in México.

Conflicts of Interest: All authors declare no conflict of interest. And all the funders had no role in the design of the study; in the collection, analyses, or interpretation of data; in the writing of the manuscript; or in the decision to publish the results.

Appendix A

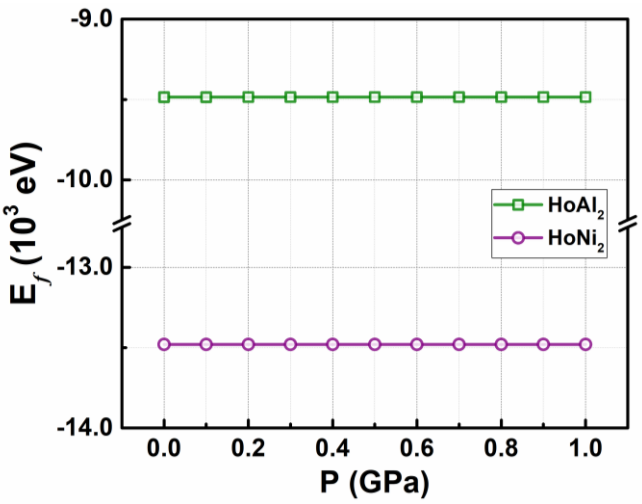

Figure A1. Calculated formation energy as a function of the applied hydrostatic pressure for ferromagnetically $HoAl_2$ and $HoNi_2$ Laves phases.

 doi:10.20944/preprints202509.0255.v1

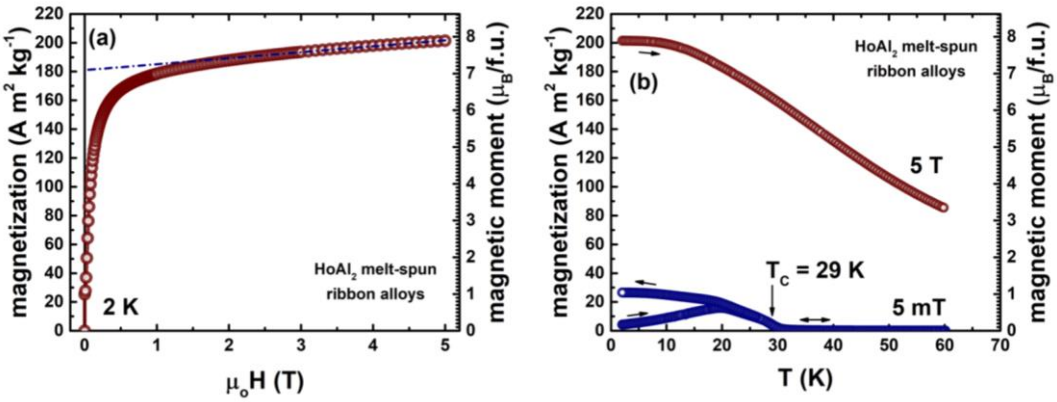

Figure A2. Magnetization isotherm at 2 K **(a)** and temperature dependence of magnetization measured under magnetic fields of 5 mT and 5 T **(b)** for $HoAl_2$ melt spun ribbons. The short-dashed line in (a) indicates the saturation magnetization extrapolated to a zero magnetic field (reported in **Table 3**). The magnetic moment per formula unit is calculated from the magnetization values. The measurements are performed in-plane along the major axis of the ribbon length using in Dynacool PPMS-VSM magnetometer. As pointed by the vertical arrow in (b), the sample shows T_C = 29 K. More experimental details can be found in reference [16].

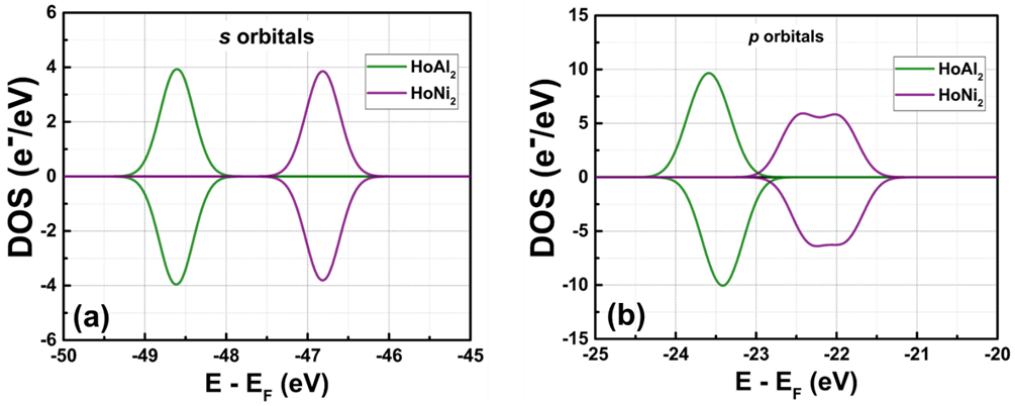

Figure A3. Partial electronic density of states at P = 0 GPa calculated for **(a)** *s* and **(b)** *p* orbitals in ferromagnetically ordered $HoAl_2$ and $HoNi_2$ Laves phases..

 doi:10.20944/preprints202509.0255.v1

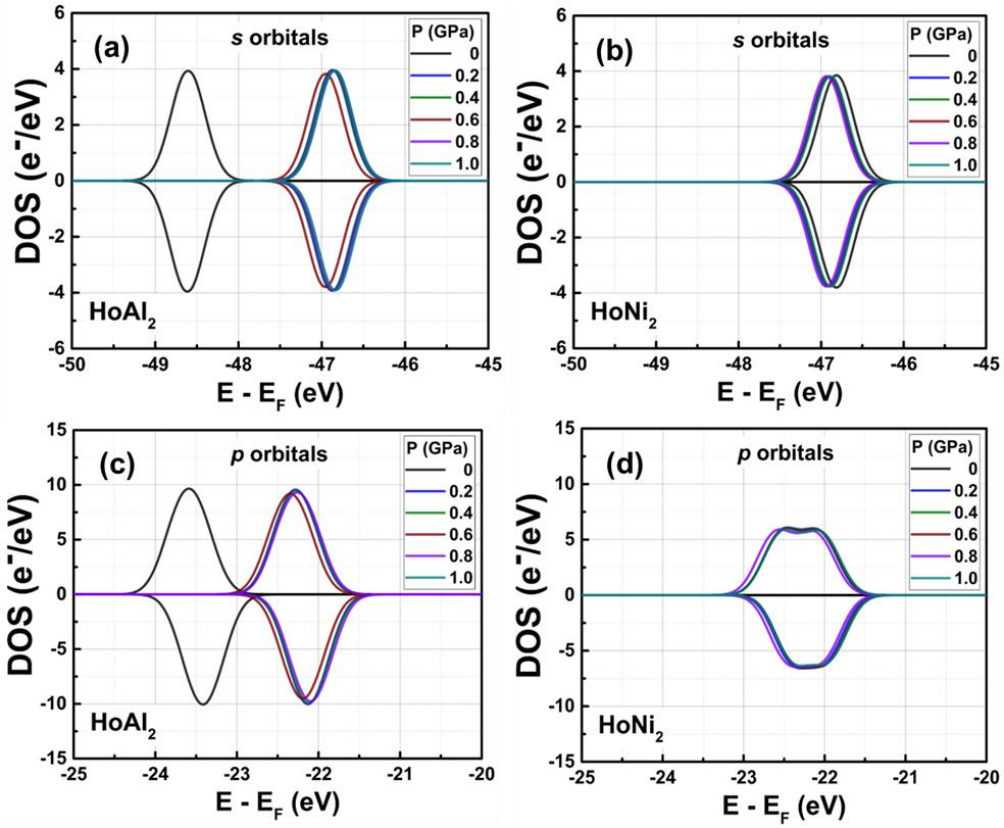

Figure A4. Partial electronic density of states calculated for *s* and *p* orbitals in ferromagnetically ordered $HoAl_2$ (**(a)**, **(c)**) and $HoNi_2$ (**(b)**, **(d)**) Laves phases within the pressure range of 0 GPa ≤ P ≤ 1.0 GPa.

References

1. Pecharsky, V.K.; Gschneider Jr., K.A. Magnetocaloric effect and magnetic refrigeration. *J. Magn. Magn. Mater.* **1999**, *200*, 044-56. DOI: https://doi.org/10.1016/S0304-8853(99)00397-2.
2. Moya, X.; Mathur, N.D. Caloric materials for cooling and heating. *Science.* **2020**, *370*, 797–803. DOI: https://doi.org/10.1126/science.abb0973.
3. Moya, X.; Kar-Narayan, S.; Mathur, N.D. Caloric materials near ferroic phase transitions. *Nature Mater.* **2014**; *14*, 439-450. DOI: https://doi.org/10.1038/nmat3951.
4. Franco, V.; Blázquez, J.S.; Ipus, J.J.; Law, J.Y.; Moreno-Ramírez, L.M.; Conde A. Magnetocaloric effect: From materials research to refrigeration devices. *Prog. Mater. Sci.* **2018**, *93*, 112-232. DOI: https://doi.org/10.1016/j.pmatsci.2017.10.005.
5. Smith, A.; Bahl, C.R.H.; Bjørk, R.; Engelbrecht, K.; Nielsen, K.K.; Pryds, N. Materials challenges for high performance magnetocaloric refrigeration devices. *Adv. Energy Mater.* **2012**, *2*, 1288-1318. DOI: https://doi.org/10.1002/aenm.201200167.
6. Pecharsky, V.K.; Gschneidner Jr., K.A. Giant magnetocaloric effect in $Gd_5(Si_2Ge_2)$. *Phys. Rev. Lett.* **1997**, *78*, 4494. DOI: https://doi.org/10.1103/PhysRevLett.78.4494.
7. Kitanovski, A. Energy applications of magnetocaloric materials. *Advanced Energy Mater.* **2020**, *10*, 1903741. DOI: https://doi.org/10.1002/aenm.201903741.
8. Lyubina, J. Magnetocaloric materials for energy efficient cooling. *J. Phys. D. Appl. Phys.* **2017**, *50*, 053002. DOI: https://doi.org/10.1088/1361-6463/50/5/053002.
9. Kotani, Y.; Takeya, H.; Lai, J.; Matsushita, Y.; Ohkubo, T.; Miura, Y.; Nakamura, T.; Hono, K. Magnetic refrigeration material operating at a full temperature range required for hydrogen liquefaction. *Nature Comm.* **2022**, *13*, 1817. DOI: https://doi.org/10.1038/s41467-022-29340-2.
10. Gschneidner Jr., K.A.; Pecharsky, V.K. Binary rare earth Laves phases - an overview. *Z. Kristallogr.* **2006**, *221*, 375-38. DOI: https://doi.org/10.1524/zkri.2006.221.5-7.375.

 doi:10.20944/preprints202509.0255.v1

11. Aschauer, U.; Braddell, R.;. Brechbuhl, S.A; Derlet, P.M.; Spaldin, N.A. Strain-induced structural instability in FeRh. *Phys. Rev. B.* **2016**, *94*, 014109. DOI: https://doi.org/10.1103/PhysRevB.94.014109.
12. He, L.; Zhu, J.; Zhang, L. First-principles study of Structural phase transition, electronic, elastic and thermodynamic properties of C15-type Laves phases $TiCr_2$ under pressure. *Physica B: Condensed Matter.* **2018**, *531*, 79-84. DOI: https://doi.org/10.1016/j.physb.2017.11.051.
13. Patel, P.D.; Shinde, S.; Gupta, S.D. First principle calculation of structural, electronic and magnetic properties of Mn_2RhSi Heusler alloy. *AIP Conf. Proc.* **2018**, *2005*, 040004. DOI: https://doi.org/10.1063/1.5050744.
14. Wang, S. First-principles prediction of ferromagnetism in transition-metal doped monolayer AlN. *Superlattices Microstruct.* **2019**, *122*, 171-180. DOI: https://doi.org/10.1016/j.spmi.2018.08.009.
15. Odkhuu, D.; Tsevelmaa, T.; Sangaa, D.; Tsogbadrakh, N.; Rhim, S.H.; Hong, S.C. First-principles study of magnetization reorientation and perpendicular magnetic anisotropy in $CuFe_2O_4$/MgO heterostructures. *Phys. Rev. B.* **2018**, *98*, 094408. DOI: https://doi.org/10.1103/PhysRevB.98.094408.
16. Sánchez Llamazares, J.L.; Zamora, J.; Sánchez-Valdés, C.F.; Álvarez-Alonso, P. Design and fabrication of a cryogenic magnetocaloric composite by spark plasma sintering based on the RAl_2 Laves phases (R = Ho, Er). *J. Alloys Compd.*, **2020**, *831*, 154779. DOI: https://doi.org/10.1016/j.jallcom.2020.154779.
17. Sánchez Llamazares, J.L.; Ibarra Gaitán, P.; Sánchez-Valdés, C.F.; Álvarez-Alonso, P.; Varga, R. Enhanced magnetocaloric effect in rapidly solidified $HoNi_2$ melt spun. *J. Alloys Compd.*, **2019**, *774*, 700-705. DOI: https://doi.org/10.1016/j.jallcom.2018.09.35.
18. Schelp, W.; Leson, A.; Drewes, W.; Purwins, H.G. Magnetization and Magnetic Excitations in $HoAl_2$. *Z. Phys. B – Condensed Matter*, **1983**, *51*, 41-47. DOI: https://doi.org/10.1007/BF01304043.
19. Gignoux, D.; Givord, F.; Lemaire, R. Magnetic properties of single crystals of $GdCo_2$, $HoNi_2$, and $HoCo_2$, *Phys. Rev. B*, 12, **1975**, 3878-3884. DOI: https://doi.org/10.1103/PhysRevB.12.3878.
20. Stein, F.; Leineweber. A. Laves phases: a review of their functional and structural applications and an improved fundamental understanding of stability and properties. *J. Mater. Sci.* **2021**, *56*, 5321-5427. DOI: https://doi.org/10.1007/s10853-020-05509-2.
21. Liu, W.; Bykov, E.; Taskaev, S.; Bogush, M.; Khovaylo, V.; Fortunato, N.; Aubert, A.; Zhang, H.; Gottschall, T.; Wosnitza, J.; Scheibel, F.; Skokov, K.; Gutfleisch, O. A study on rare-earth Laves phases for magnetocaloric liquefaction of hydrogen. *Appl. Mat. Today.* **2022**, *29*, 101624. DOI: https://doi.org/10.1016/j.apmt.2022.101624.
22. Gschneidner, K.A. Jr; Pecharsky, V.K.; Tsokol, A.O. Recent developments in magnetocaloric materials. *Rep. Prog. Phys.* **2005**, *68*, 1479. DOI: https://doi.org/10.1088/0034-4885/68/6/R04.
23. Kumar K.S.; Hazzledine, P. M. Polytypic transformations in Laves phases. *Intermetallics*. **2004**, *12*, 763-770. DOI: https://doi.org/10.1016/j.intermet.2004.02.017.
24. Biswas, A.; Pathak, A.K.; Zarkevich, N.A.; Liu, X.; Mudryk, Y.; Balema, V.; Johnson, D.D.; Pecharsky, V.K. Designed materials with the giant magnetocaloric effect near room temperature. *Acta Materialia*. **2019**, *180*, 341-348. DOI: http://doi.org/10.1016/j.actamat.2019.09.023.
25. Kikugawa, N.; Kato, T.; Hayashi, M.; Yamaguchi, H. Single-Crystal Growth of a Cubic Laves-Phase Ferromagnet $HoAl_2$ by a Laser Floating-Zone Method. *Crystals*, **2023**, *13*, 760. DOI: https://doi.org/10.3390/cryst13050760.
26. de Souza, M.V.; Plaza, E.J.R.; Campoy, J.C.P. Anisotropic magnetoresistivity and magnetic entropy change in $HoAl_2$. *Intermetallics*, **2016**, *715*, 51-53. DOI: https://doi.org/10.1016/j.intermet.2016.05.005.
27. Gil, L.A.; Campoy, J.C.P.; Plaza, E.J.R.; de Souza, M.V. Conventional and anisotropic magnetic entropy change in $HoAl_2$ ferromagnetic compound. *JMMM*, **2016**, *409*, 45-49. DOI: https://dx.doi.org/10.1016/j.jmmm.2016.02.085.
28. Ibarra, M.R.; Moze, O.; Algarabel, P.A.; Arnaudas, J.I.; Abell, J.S.; del Moral, A. Magnetoelastic behavior and the spin-reorientation transition in $HoAl_2$. *J. Phys. C: Solid State Phys.*, **1988**, *21*, 2735-2748. DOI: https://doi.org/10.1088/0022-3719/21/14/013.
29. Cococcioni, M.; de Gironcoli, S. Linear response approach to the calculation of the effective interaction parameters in the LDA+U method. *Phys. Rev. B.* **2005**, 71, 035105. DOI: https://doi.org/10.1103/PhysRevB.71.035105.

 doi:10.20944/preprints202509.0255.v1

30. Anisimov, V.I.; Zaanen, J.; Andersen; O.K. Band theory and Mott insulators: Hubbard *U* instead of Stoner *I*. *Phys*. *Rev*. *B*. **1991**, 44, 943. DOI: https://doi.org/10.1103/PhysRevB.44.943.
31. Moroni, E.G.; Kresse, G.; Hafner, J.; Furthmüller, J. Ultrasoft pseudopotentials applied to magnetic Fe, Co, and Ni: From atoms to solids. *Phys*. *Rev*. *B*. **1997**, 56, 15629. DOI: https://doi.org/10.1103/PhysRevB.56.15629.
32. Hafner, J.; Wolverton, C.; Ceder, G. Toward computational materials design: the impact of density functional theory on materials research. *MRS Bulletin*. **2006**, *31*, 659-668. DOI: https://doi.org/10.1557/mrs2006.174.
33. Staroverov, V. N.; Scuseria, G. E.; Tao, J.; Perdew, J. P. Test of the ladder of density functionals for bulk solids and surfaces. Phys. Rev. B. **2004**, *69*, 075102. DOI: https://doi.org/10.1103/PhysRevB.69.075102.
34. Lewars, E. Computational chemistry: introduction to the theory and applications of molecular and quantum mechanics. First edition, **2004**. ISBN: 0-306-48391-2, Print ISBN: 1-4020-7285-6.
35. Clark, S.J.; Seagall, M.D.; Pickard, C.J.; Hasnip, P.J.; Probert, M.I.J.; Refson, K.; Payne, M.C. First principles methods using CASTEP. *Z. Kristallogr*. **2005**, *220*, 567-570. DOI: https://doi.org/10.1524/zkri.220.5.567.65075.
36. Bader, R.F.W. The density in density functional theory. *J. Molec. Struct.: THEOCHEM*. **2010**, *943*, 2-18. DOI: https://doi.org/10.1016/j.theochem.2009.10.022.
37. Monkhorst, H.J.; Pack, J.D. Special points for Brillouin-zone integrations, *Phys. Rev. B*. **1976**, *13*, 5188. DOI: https://doi.org/10.1103/PhysRevB.13.5188.
38. Villars, P.; Cenzual, K.; Okamoto, H.; Hulliger, F.; Iwata, S. $HoNi_2$ Crystal Structure: Datasheet from "PAULING FILE MULTINARIES EDITION – 2012". Springer Materials.
39. Tipler, P.A.; Llewellyn, R. *Modern Physics*, 5th ed.; W.H. Freeman and Company: New York, NY, USA, 2008; ISBN 13 978-0-7167-7550-8/10 0-7167-7550-6.
40. Cyrot, M.; Lavagna, M. Density of states and magnetic properties of the rare-earth compounds RFe_2, RCo_2 and RNi_2. *Le Journal de Physique*. **1979**, *40*, 763. DOI: https://doi.org/10.1051/jphys:01979004008076300.
41. von Ranke, P.J.; Pecharsky, V.K.; Gschneidner, K.A. Jr.; Influence of the crystalline electrical field on the magnetocaloric effect of $DyAl_2$, $ErAl_2$ and $DyNi_2$. *Phys. Rev. B*, 58, **1998**, 12110. DOI: https://doi.org/10.1103/PhysRevB.58.12110.
42. de Oliveira, I.G.; Garcia, D.C.; von Ranke, P.J.; Spin reorientation and magnetocaloric effect study in $HoAl_2$ by a microscopic model Hamiltonian. *J. Appl. Phys.* 102, **2007**, 073907. DOI: https://doi.org/10.1063/1.2783781.
43. Campoy, J.C.P.; Plaza, E.J.R.; Coelho, A.A.; Gama, S.; Magnetoresistivity as a probe to the field-induced change of magnetic entropy in RAl_2 compounds (R=Pr,Nd,Tb,Dy,Ho,Er). Phys. Rev. B, 74, **2006**, 134410. DOI: http://doi.org/10.1103/PhysRevB.74.134410.
44. Taylor, K.N.R.; Intermetallic rare-earth compounds. *Advances in Physics*, **1971**, *20*, 551-660. DOI: https://doi.org/10.1080/00018737100101311.
45. Farrell, J.; Wallace, W.E.; Magnetic properties of intermetallic compounds between the lanthanides and nickel or cobalt. *Inorg. Chem.*, **1966**, 5, 1, 105–109. DOI: https://doi.org/10.1021/ic50035a025